

Au Clusters on Pd Nanosheets Selectively Switch the Pathway of Ethanol Electrooxidation: Amorphous/Crystalline Interface Matters

Fan Lv, Weiyu Zhang, Mingzi Sun, Fangxu Lin, Tong Wu, Peng Zhou, Wenxiu Yang, Peng Gao, Bolong Huang,* and Shaojun Guo*

The development of ethanol electrooxidation catalysts with high activity and robust stability is essential for the commercialization of direct ethanol fuel cells. However, because of their low C1 selectivity, the electrocatalytic efficiency of catalysts for complete ethanol oxidation is still far from satisfying. Herein, a novel 2D Pd–Au heterogeneous catalyst for enhancing C1 selectivity to achieve highly efficient ethanol oxidation through phase and interphase engineering is designed. It is found that owing to the plentiful amorphous/crystalline interphases, the selectivity of C1 pathway on Pd–Au heterocatalyst can be improved up to 33.2% at a low potential, 10.4 times higher than commercial Pd/C (3.2%). Furthermore, 89.1% of initial mass activity of Pd–Au HNS can be retained after the accelerated degradation test of 2000 potential cycles, much higher than those of Pd NS (39.3%), commercial Pd/C (34.4%), and Pt/C (11.4%). The CO stripping and in situ Fourier transform infrared experiments reveal that 2D Pd–Au heterocatalyst, with intricate design of the amorphous Pd domain and the crystalline Au cluster interface, has better antipoisoning properties and stronger C–C bond cleavage ability than pure Pd nanosheets. Density functional theory calculations further demonstrate that the introduction of Au clusters switches on the electroactivity of amorphous Pd as the electron pump to accomplish the complete oxidation of ethanol, in which the selectivity for C1 pathway is significantly boosted whereas the typical C2 pathway is substantially blocked.

1. Introduction

Direct liquid fuel cells have been recognized as a promising future energy device with high energy/power density, fuel flexibility, and environmental friendliness.^[1,2] Among all kinds of the liquid fuels, ethanol is of great advantages including large volume energy density (6.34 kWh L⁻¹), low toxicity, and easy accessibility from biomass.^[3–5] Therefore, direct ethanol fuel cells (DEFCs) have received great attention in recent years. However, the lack of active and durable anode electrocatalysts for ethanol oxidation reaction (EOR) becomes a severe challenge.^[4,6] So far, Pt- and Pd-based materials are the most favorable catalysts for EOR.^[7–12] Nonetheless, insufficient activity and poor stability have still impeded their further utilization.^[13,14] The essential problem of these EOR catalysts is their incomplete oxidation of ethanol with only four electrons transfer, named C2 pathway, resulting in the formation of acetic acid or acetate as the final products.^[15] Inversely, the preferred C1 pathway that produces CO₂ or carbonate with 12 electrons transfer is greatly hindered because of high energy barrier of C–C bond cleavage and strongly adsorbed intermediate species such as CO_{ad} and –CH_x.^[5,16,17] The reported EOR selectivity of Pt and Pd for C1 pathway has been uncovered to be very low (<75%).^[13,18] Thus, constructing active and durable EOR catalysts with high selectivity for C1 pathway is of great significant.


Generally, there are two common strategies that have been applied to design efficient Pt- or Pd-based electrocatalysts toward EOR. The first one is introducing an oxyphilic component by alloying or recombination, which includes Ni, Co, Ru, Rh, Ir, Sn metal as well as metal oxides/hydroxide like TiO₂, CeO₂, Ni(OH)₂, etc.^[5,9,19–23] The enhanced catalytic performance boosted by these oxyphilic components can be mainly attributed to the bifunctional mechanism. The easily adsorbed OH_{ads} on these oxyphilic sites of the catalysts is beneficial to the removal of CO and –CH_x species, thus promoting the ethanol oxidation efficiency.^[3,24] The second strategy is to modify the electronic structure of Pd or Pt by doping another metal like Au, Ag or no metal like P and so on, therefore weakening the affinity for

CO and –CH_x species, thus promoting the ethanol oxidation efficiency.^[3,24] The second strategy is to modify the electronic structure of Pd or Pt by doping another metal like Au, Ag or no metal like P and so on, therefore weakening the affinity for

F. Lv, W. Zhang, K. Wang, F. Lin, Dr. P. Zhou, J. Hou, Dr. W. Yang, Prof. S. Guo
School of Materials Science and Engineering
College of Engineering
Peking University
Beijing 100871, P. R. China
E-mail: guosj@pku.edu.cn

M. Sun, T. Wu, Prof. B. Huang
Department of Applied Biology and Chemical Technology
The Hong Kong Polytechnic University
Hung Hom, Kowloon, Hong Kong SAR 999077, China
E-mail: bhuang@polyu.edu.hk

Prof. P. Gao
Electron Microscopy Laboratory, and
International Center for Quantum Materials
School of Physics
Peking University
Beijing 100871, China

 The ORCID identification number(s) for the author(s) of this article can be found under <https://doi.org/10.1002/aenm.202100187>.

DOI: 10.1002/aenm.202100187

poisonous adspecies through synergistic effects and electronic effects, thus facilitating higher CO₂ selectivity.^[7,25–28] However, owing to the complexity of EOR process involving various influential species, an ideal electrocatalyst should at least have: i) active sites for C–C bond breaking; ii) the selective surface sites for CO₂ formation; iii) ability for the removal of poisonous adspecies.^[13,24,29] In this regard, new strategies for tuning the surface and interphase of the EOR catalysts, like composition, structure, and electronic states, to selectively switch the pathway of ethanol electrooxidation are highly required, and to achieve this, more elaborately rational design of catalysts is of remarkable importance.

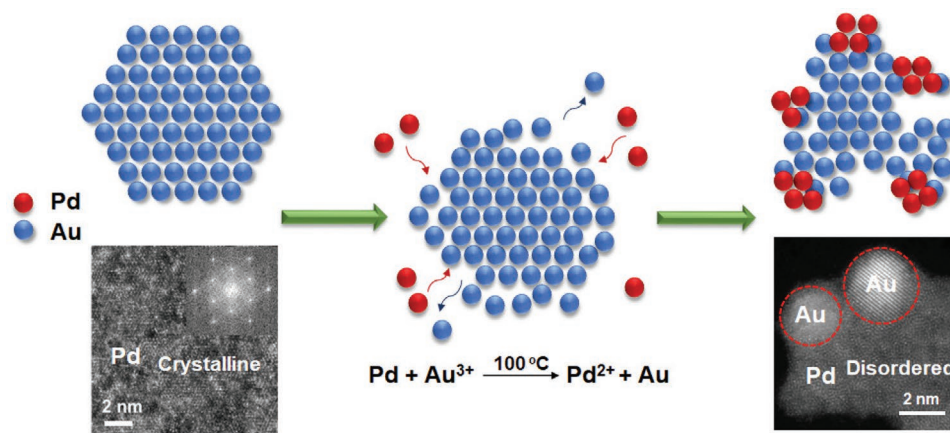
Herein, we present a new method for making a novel 2D Pd–Au heterophase nanosheet catalyst (Pd–Au HNS) with abundant amorphous Pd domain/crystalline Au cluster interphase for achieving superior EOR catalysis with much higher selectivity for the C1 pathway. With beyond ten times improvement of the C1 pathway selectivity relative to that of commercial Pd/C, the synthesized Pd–Au HNS exhibits excellent EOR activity with a mass activity of 9.1 A mg⁻¹_{Pd}, 9.3 times higher than that of commercial Pd/C. Meanwhile, Pd–Au HNS exhibits the long-term stability by showing the little decay after the accelerated degradation test (ADT) of 2000 potential cycles and repeatedly chronoamperometry (CA) test. The CO stripping, analysis of EOR product, and in situ Fourier transform infrared (FTIR) experiments reveal that the Pd–Au HNS has better antipoisoning property and stronger C–C bond cleavage ability than pure Pd NS and commercial Pd/C, which are the origin for greatly enhanced EOR activity and durability of Pd–Au HNS. Further supported by the density functional theory (DFT) calculation, the typical crystalline Pd NS shows an even electroactivity that strongly prefers the four-electron C2 pathway of EOR. By introducing the Au, the resultant amorphization of Pd significantly activates the electroactivity of Pd at the interfacial region. Au clusters also highly facilitate alleviating the energy barriers of electrons transfer from adsorbates to achieve the 12-electron C1 pathway.

2. Results and Discussion

The Pd–Au HNS with abundant amorphous Pd domain/crystalline Au cluster interphase was synthesized through a

two-step strategy. First, the thin Pd NS was prepared by the reduction of Pd(acac)₂ in the presence of NH₄Br and W(CO)₆ in oleylamine (OAM). Because the redox potential of AuCl₄⁻/Au (1.5 V vs RHE) is more positive than PdCl₄²⁻/Pd (0.95 V vs RHE),^[30] the Pd–Au HNS could be further created through a simple galvanic reaction between Pd NS and [AuCl₄]⁻ ion (details in the Experimental Section). As illuminated in **Scheme 1**, the corrosion reaction between [AuCl₄]⁻ ions with Pd atoms of low coordination numbers at the edge of Pd NS^[31,32] could break the initial long-range ordered Pd crystalline structure, resulting in the formation of unique amorphous/crystalline Pd–Au hetero-interphase. Different from the initial hexagonal Pd NS (**Figure 1a**), the edge of Pd–Au HNS became irregular and was decorated with many dark nanoclusters, similar to lots of tentacles (**Figure 1b**). The lateral size of the Pd–Au NSs is about 25–50 nm, and the thickness measured from the wrinkled Pd–Au NS is about 1.8 nm (inset in **Figure 1b**). The aberration-corrected high-angle annular dark-field scanning transmission electron microscopy (HAADF-STEM) was performed to further reveal the atomic-scale interphase of Pd–Au HNS. The bright part of one individual Pd–Au NS in dark-field model is Au since Au has larger molecular weight than Pd (**Figure 1c**). Interestingly, observed from the disordered lattice fringes and diffuse rings in the selected-area fast Fourier transformation (FFT) patterns (**Figure 1d,e**), the outer edge part of Pd, which is around the Au nanocluster, turns into amorphous. Inversely, the Au nanocluster is totally crystalline. To be noted, the inner part of the Pd is still crystalline (**Figure S1**, Supporting Information), indicating the Au-induced amorphization of Pd here owing to the strong electron pulling ability of Au. The hetero-interphase structure of Pd–Au HNS was also proved by the element distribution of Pd and Au using STEM energy-dispersive X-ray spectroscopy (EDS) mapping (**Figure 1f**). The composition ratio of Pd to Au in Pd–Au HNS determined by TEM-EDS is about 88.0/12.0 (**Figure S2**, Supporting Information), which is similar to the results of inductively coupled plasma optical emission spectrometry (ICP-AES) (**Table S1**, Supporting Information). The ratio of Au:Pd can be adjusted from 8% to 19% by adding different amount of Au precursor (**Figures S3 and S4**, Supporting Information).

Powder X-ray diffraction (PXRD) patterns show that both Pd–Au HNS and Pd NS have a face centered cubic (fcc)



Scheme 1. Schematic illustration of the evolution process from crystalline Pd NSs to Pd–Au HNS with abundant Au NPs/disordered Pd matrix interface.

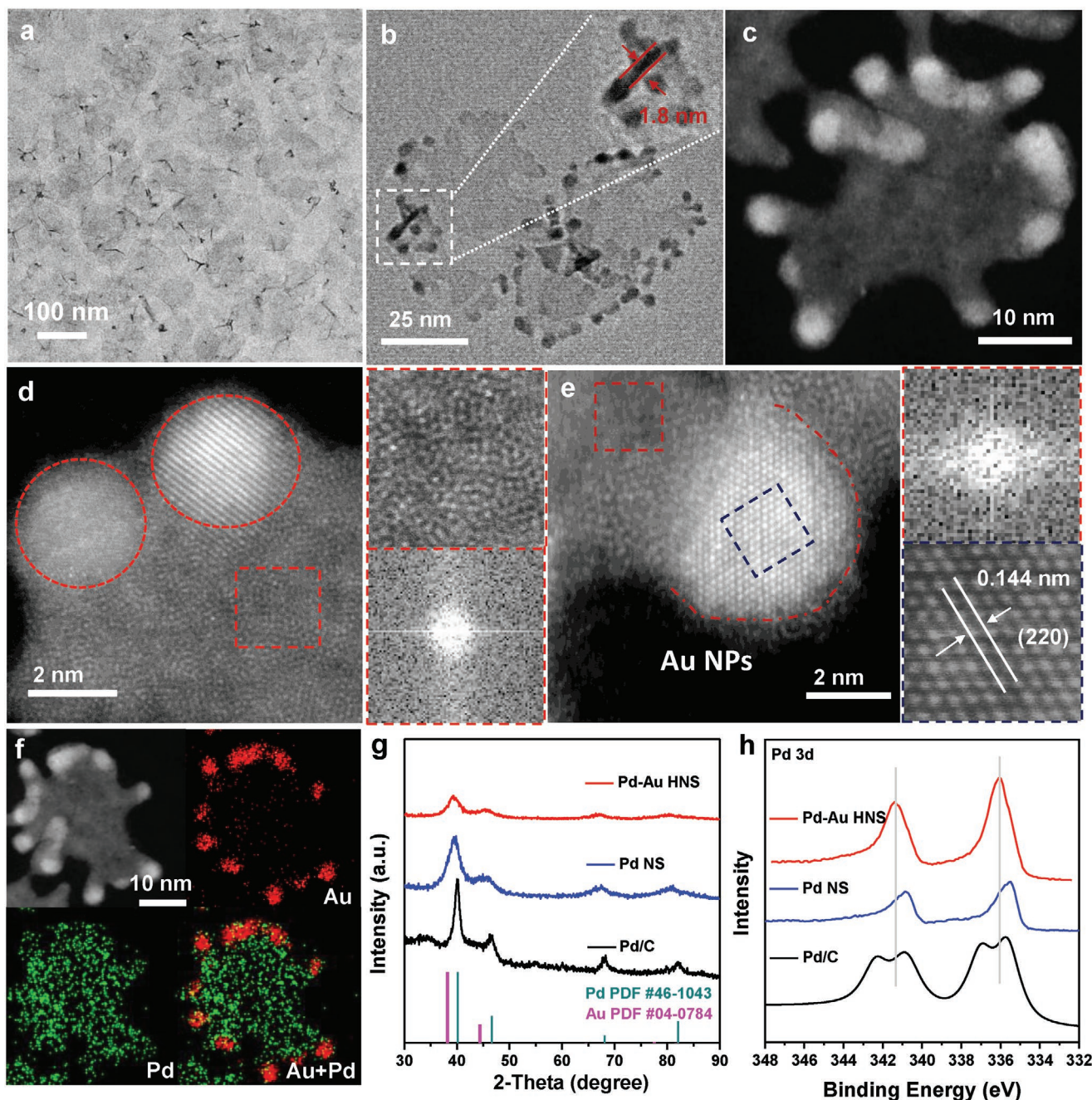


Figure 1. Phase and structure characterization of 2D Pd–Au HNS. a) TEM image of Pd NSs, b) TEM image of 2D Pd–Au HNS, c–e) HAADF-STEM images and f) elemental EDS-mapping of Pd–Au HNS. g) XRD patterns and h) XPS spectra of Pd 3d of Pd–Au HNS, Pd NS, and commercial Pd/C.

structure (Figure 1g). Compared with commercial Pd/C, the Pd NS has the higher lattice parameter by showing the negatively shifted diffraction peaks. By introducing Au in the Pd NS, the peaks do not continue to shift negatively, revealing the Pd–Au HNS is the heterogeneous phase but not the alloy phase. The diffraction peaks of fcc Au are not observed owing to the small size and relatively low amount of Au nanoclusters. Moreover, the diffraction peaks become broad with the weakened intensity, further demonstrating the partial amorphization in the Pd–Au HNS. The Pd–Au HNS was also studied by Pd K-edge extended X-ray absorption fine structure (EXAFS) to understand

the coordination environment change of Pd to uncover the disorder transform process (Figure S5 and Table S2, Supporting Information). The Pd–Pd bond in Pd–Au HNS is 2.81 Å, larger than that in Pd NS (2.76 Å), being in accordance with the bond length of other reported amorphous Pd.^[33] X-ray photoelectron spectroscopy (XPS) was conducted to confirm the presence of Pd and Au and their electronic interaction in Pd–Au HNS (Figure 1h and Figure S6, Supporting Information). We found that the Pd and Au in Pd–Au HNS are mainly metallic state. The obvious positive shift of the two Pd 3d XPS peaks of Pd–Au HNS relative to those of Pd NS and commercial

Pd–C indicates the electron transfer from Pd domain to the Au cluster at the interphase.

Before studying their electrocatalytic properties of toward EOR, the carbon-supported Pd–Au HNS and crystalline Pd NS were first made by sonicating the mixture of HNS with commercial carbon in organic solvent (denoted as Pd–Au HNS/C and Pd NS/C, respectively). The cyclic voltammetry (CVs) of different catalysts were recorded in N₂-saturated 1 M KOH (Figure S7, Supporting Information). We found that the Pd–Au HNS/C with different Pd/Au composition all show better EOR activity than Pd NS/C (Figure S8, Supporting Information). Among them, the Pd–Au HNS/C with Pd/Au atomic ratio of 88:12 shows the best mass activity of 9.1 A mg⁻¹_{Pd} (8.0 A mg⁻¹_{Pd+Au}, Figure S9, Supporting Information) and an excellent specific activity of 11.5 mA cm⁻² toward EOR, which is 2.3, 7.0, and 9.3 times higher mass activity, and 2.9, 6.6, and 4.1 times higher specific activity than those of pure crystalline Pd NS/C, commercial Pt/C, and Pd/C, respectively (Figure 2a,b). Therefore, the introduction of suitable Au nano-clusters in the Pd NS indeed greatly enhances the electrocatalytic activity toward EOR. Moreover, the ratio of current peak in the forward scan (*I_f*) to backward scan (*I_b*) in EOR curves represents the anti-poisoning ability of the catalysts for removing the intermediate carbonaceous species on active sites.^[34–36] The *I_f*/*I_b* ratio of Pd–Au HNS/C is 1.45, larger than those of Pd NS/C (1.22), commercial Pd/C (0.76), and Pt/C (1.21), suggesting the higher CO poison resistance in Pd–Au HNS/C. Furthermore, the CO oxidation peak of Pd–Au HNS/C shows the negative shift of 80 and 116 mV in comparison with those of Pd NS and commercial Pd/C in the CO stripping test, verifying the anti-CO poisoning of Pd–Au HNS/C (Figure S10, Supporting Information).

We further studied the catalytic stability of Pd–Au HNS/C toward EOR. After 2000 continuous cycles, more than 89.1% of initial mass activity of Pd–Au HNS can be retained, much higher than those of Pd NS/C (39.3%), commercial Pd/C (34.4%), and Pt/C (11.4%) (Figure 2c and Figure S11, Supporting Information). Meanwhile, the CA curves of Pd–Au HNS/C show the slowest decline, in contrast with the sharp drops of commercial Pd/C and Pt/C (Figure 2d). The Pd–Au HNS/C maintain a specific current of 299 mA mg⁻¹ after 5000 s stability test, more than two times higher than Pd NS. In addition, after consecutive four cycles CA tests, the catalytic activity of Pd–Au HNS/C can be recovered by replacing fresh working electrolyte (Figure 2e). TEM and XRD analyses after CA tests further confirm that the structure and phase of Pd–Au HNS/C stayed can be well maintained (Figures S12 and S13, Supporting Information).

To gain deep insight into the enhanced catalytic performance on the Pd–Au HNS/C, we used in situ FTIR spectroscopic study on the Pd–Au HNS/C and pure Pd NS/C (Figure 3a,b). In the observed spectra, two upward IR bands at 1045 and 1085 cm⁻¹ can be attributed to the C–O stretching vibration of ethanol, indicating the consumption of ethanol in oxidation.^[37,38] Other three distinct downward peaks at 1551, 1415, and 1348 cm⁻¹ can be assigned to the produced acetate ion (CH₃COO⁻), corresponding to the asymmetric, symmetric stretching band of O–C–O, and bending vibration of –CH₃ in acetate.^[20,21,39–41] The ethanol oxidation in Pd–Au HNS/C occurred at a more

negative potential than Pd HNS/C, revealing its accelerated reaction kinetics. In addition, the band of CO₃²⁻ is located at 1390 cm⁻¹, which is overlapped with the peaks at 1415 cm⁻¹ assigned to acetate. Therefore, we could roughly distinguish the existence of CO₃²⁻ by simply comparing the intensity ratio change of the band at ≈1415 and 1551 cm⁻¹.^[38,39,42] In the in situ FTIR spectrum on Pd–Au HNS/C, the intensity ratio of these two bands is obviously higher than that on Pd NS/C, resulting from the more CO₃²⁻ in the electrolyte (generated CO₂ dissolved in alkaline media). It indicates the formation of CO₂ from the C–C band break of ethanol by following the C1 pathway. More importantly, the peak attributed to CO₃²⁻ ion also appeared at low potentials in the FTIR spectra of Pd–Au HNS/C, different from previous reports that the C–C band cleavage on Pd-based catalyst only took place at relative high potential.^[37] Moreover, a weak peak at 2343 cm⁻¹, belonging to CO₂ (O–C–O asymmetric stretching), emerged at high potentials for Pd–Au HNS/C, but the peak did not appear on Pd HNS, which indicates that most KOH in the thin-layer solution was neutralized by large amount of formed CO₂ in Pd–Au HNS/C system while the local pH drops to the value lower than 6.3. Therefore, the selectivity of C1 pathway for CO₂ production is obviously enhanced in Pd–Au HNS/C compared with that in pure Pd NS/C. We confirm the stronger ability of C–C bond cleavage toward EOR on Pd–Au HNS/C.

To get more precise EOR selectivity of these catalysts, we analyze the oxidation product after long-term CA tests at two different potentials by high-performance liquid chromatography (HPLC). Figure 3c,d shows the calculated C2 and deduced C1 selectivity of these Pd-based catalysts. At a low potential at 0.5 V versus RHE, the Faradic efficiency (FE) for EOR of Pd–Au HNS/C can even reach up to 33.2%, outperforming those of Pd NS/C (5.9%) and commercial Pd/C (3.2%), as well as some recently reported Pd-based EOR catalysts (Table S3, Supporting Information). As the applied potential reaches 1.0 V, the C1 selectivity on Pd–Au HNS/C still presents a high value of 17.6%, much higher than those of Pd NS/C (4.1%) and Pd/C (3.6%). This indicates the C–C band cleavage (the necessary steps in C1 pathway) is much improved on Pd–Au HNS/C than that on Pd NS/C, thus enhancing the activity for EOR on Pd–Au HNS/C.

We have further explored the origin for the selectivity enhancement of complete EOR process by the adoption of Au cluster on Pd NS by theoretical calculation. The uniform distribution of bonding and antibonding near the Fermi level (*E_F*) endows the even charge transfer ability on the Pd NS surface (Figure 4a). With the introduction of the Au cluster on Pd NSs, the evident distortion of the structure leads to the amorphization of Pd, in accordance with our experiment results. The interfacial (IF) construction endows the electron-rich character near the IF region, representing the selectivity modulation on a different region of Pd–Au HNS (Figure 4b). To gain more insight into the electronic properties, we further interpret the projected partial density of states (PDOS) of key intermediates to illustrate the selectivity modulations. Notably, the surface Pd and bulk Pd shows a broad 4d band covering from 6 eV below *E_F* to *E_F*. Moreover, the d-band-center position remains similar, indicating a less electroactivity preference. The broadband feature of Pd-4d ensures the preferred

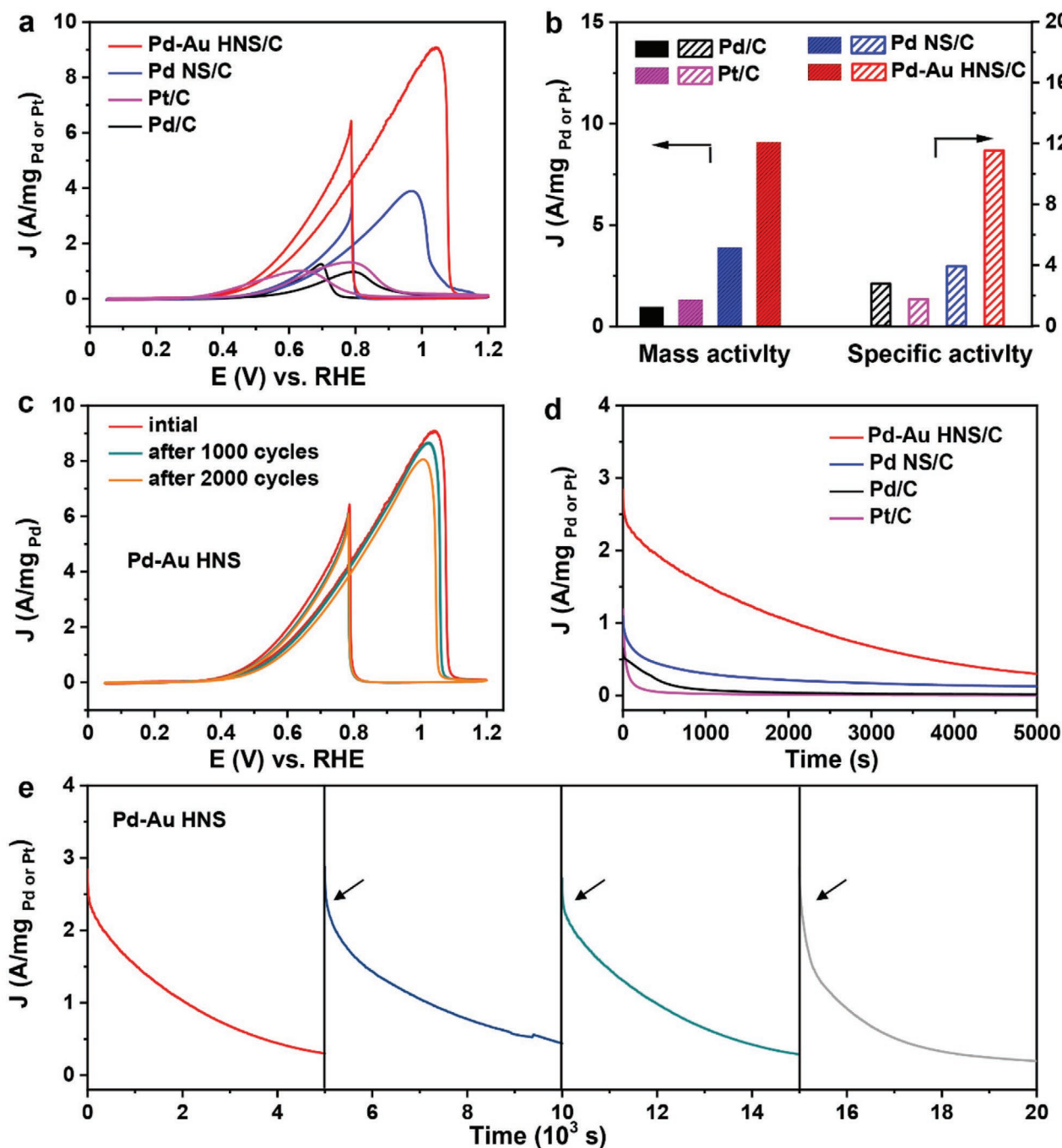


Figure 2. EOR performance of different electrocatalysts. a) Mass-normalized EOR CVs, b) histogram of specific and mass activities for EOR at peak potentials, c) mass activities of Pd–Au HNS/C after different scan cycles, d) chronoamperometric (CA) tests of EOR, e) long-time durability of Pd–Au HNS/C, and the arrows indicate when the electrolyte is refreshed.

adsorption of $\text{CH}_3\text{CH}_2\text{OH}$ and CH_3CO , which guarantees a good start of the electrocatalysis (Figure 4c). Both CO and CO_2 are preferred at the bridge top position of Pd NSs surface. However, an evident gap between adsorbate orbitals and Pd-4d orbitals is noted, demonstrating a barrier for electron transfer toward Pd, which well explained the ultralow selectivity of C1 reaction pathway for EOR. The much more involved electrons in C1 pathway are hindered by the electron transfer

gap initiated at CO (Figure 4d). In comparison, the adoption of the Au cluster largely activates the Pd orbital toward E_F , which leads to a selectivity differentiation on Pd–Au HNS between the IF region and the bulk amorphous Pd. The “electron pumping” ability of Pd is activated by the IF Au, in which the amorphous structure also reduces the Coulomb repulsion for electron transfer (Figure 4e). The site-dependent PDOS of Au represents a broadband electron-rich feature near the IF

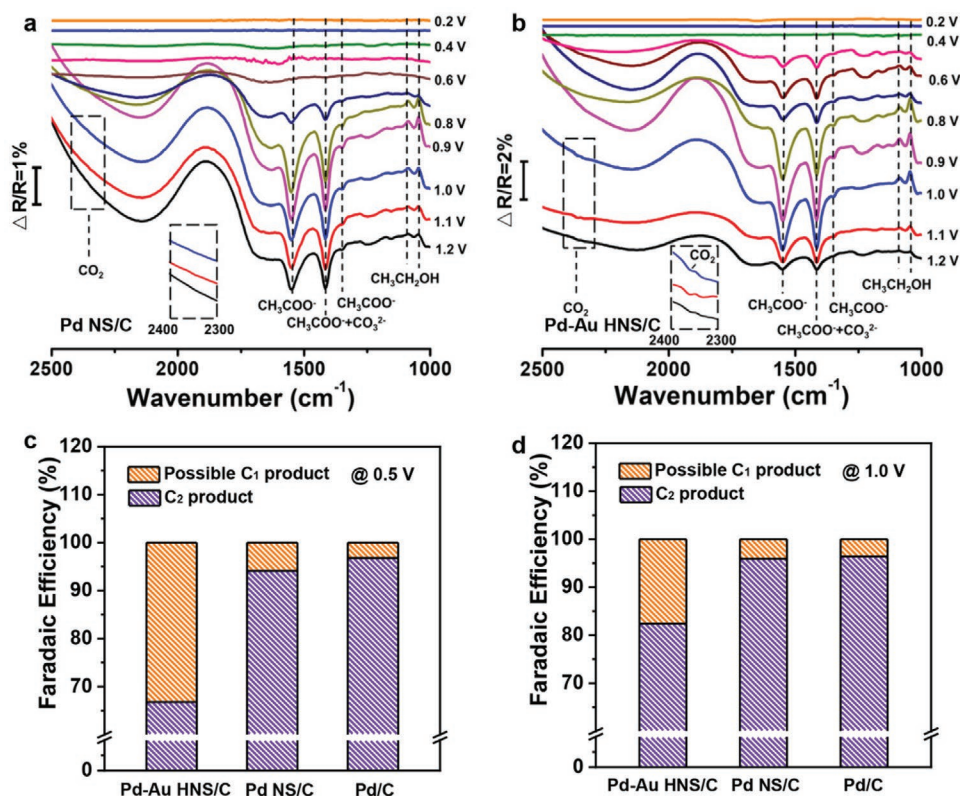


Figure 3. EOR selectivity of Pd–Au HNS. a,b) In situ FTIR spectrum of EOR on Pd NS and Pd–Au HNS at different potentials varying from 0.20 to 1.2 V at an interval of 0.1 V in 0.1 M KOH + 1 M ethanol solution. Insets show the enlarged areas marked with dashed line boxes from 2400 to 2300 cm⁻¹. c,d) Faradaic efficiency of C₂ product and deduced C₁ products on Pd–Au HNS, Pd NS, and commercial Pd/C at 0.5 and 1.0 V.

region, demonstrating a good electron acceptor from adsorbates. As Au is far from the IF region, the 5d bands immediately downshift toward E_V 3 eV, which indicates the induced unique electronic structure by interfacial coupling between Pd and Au (Figure 4f). Thus, we move to the adsorption of key intermediates to further demonstrate the role of Au cluster in Pd–Au HNS. For the key oxidation step of CH₃ in C1 pathway, the Au at IF region is playing a critical role in alleviating the gap between CH₃ toward Pd, supporting a much-enhanced oxidation process for the formation CO. For CO adsorption, such gap shows a similar size as on the Pd NSs, which represents the existence of an energy barrier for the final oxidation step of CO (Figure 4g). In comparison, the Au at IF region contributes very limited assistance in electron transfer for the oxidation of CH₃CO. Instead, the strong p–d coupling between Au-5d and CH₃CO-2p results in an easy C–C bond cleavage for C1 pathway. The adsorption of CH₃COO demonstrates a strong p–d coupling with strong binding, which lowers the conversion efficiency of the C2 route (Figure 4h).

From the energetic view, the free energy diagrams of C1 and C2 reaction pathway in Pd NS and Pd–Au HNS in alkaline conditions are plotted to gain insight into the C1 selectivity enhancement on Pd–Au HNS (Figure 5). For the Pd NS, the C1 reaction pathway is severely hindered by the two substantial energy barriers in the last two consecutive oxidation steps, especially the CH₃ oxidation. The largest barrier for C1 pathway is 1.73 eV. Moreover, the free energies of CO and CO₂

are higher than that of ethanol at $U = 0$ V, suggesting the C1 pathway is highly thermodynamically unfavorable, supporting the ultralow selectivity in experiments. The C1 pathway of Pd NS suffers from the insignificant energy gain in the CH₃CO to CH₃ and CO step, which indicates the inability of Pd NS in breaking the C–C bond in acidic condition. The free energy change in the C–C bond scissoring step is fixed and cannot be modulated by adjusting external potential, as the “death zone” of EOR catalysis. The “death zone” indicates that the ability to break the C–C bond is an intrinsic property of the catalyst material. On the other hand, the alkaline C1 pathway also suffers from the low reactivity for the first oxidation step and insufficient energy gain in the formation of CO₂ at the theoretical onset potential $U = 0.35$ V. The insufficient energy gain might lead to incomplete reaction and finally the possible poisoning of CO (Figure 5a). The C2 reaction pathway for Pd NS is much easier to proceed as the activation barriers of only two electrons transfer in the oxidation of CH₃CO to CH₃COO/CH₃COO are much smaller than the five-electron oxidation [CH₃ → CO] in the C1 pathway. Thus, the activation barriers in C2 pathway can be considered as the selectivity switch (Figure 5b). After incorporating Au clusters on the amorphous Pd nanosheets, the EOR activity and C1 selectivity are significantly enhanced, demonstrating a much smaller energy barrier in the CH₃ oxidation step, in which the barriers have reduced to 0.56 eV. Moreover, the total reaction becomes exothermic. The C–C bond scissoring ability is

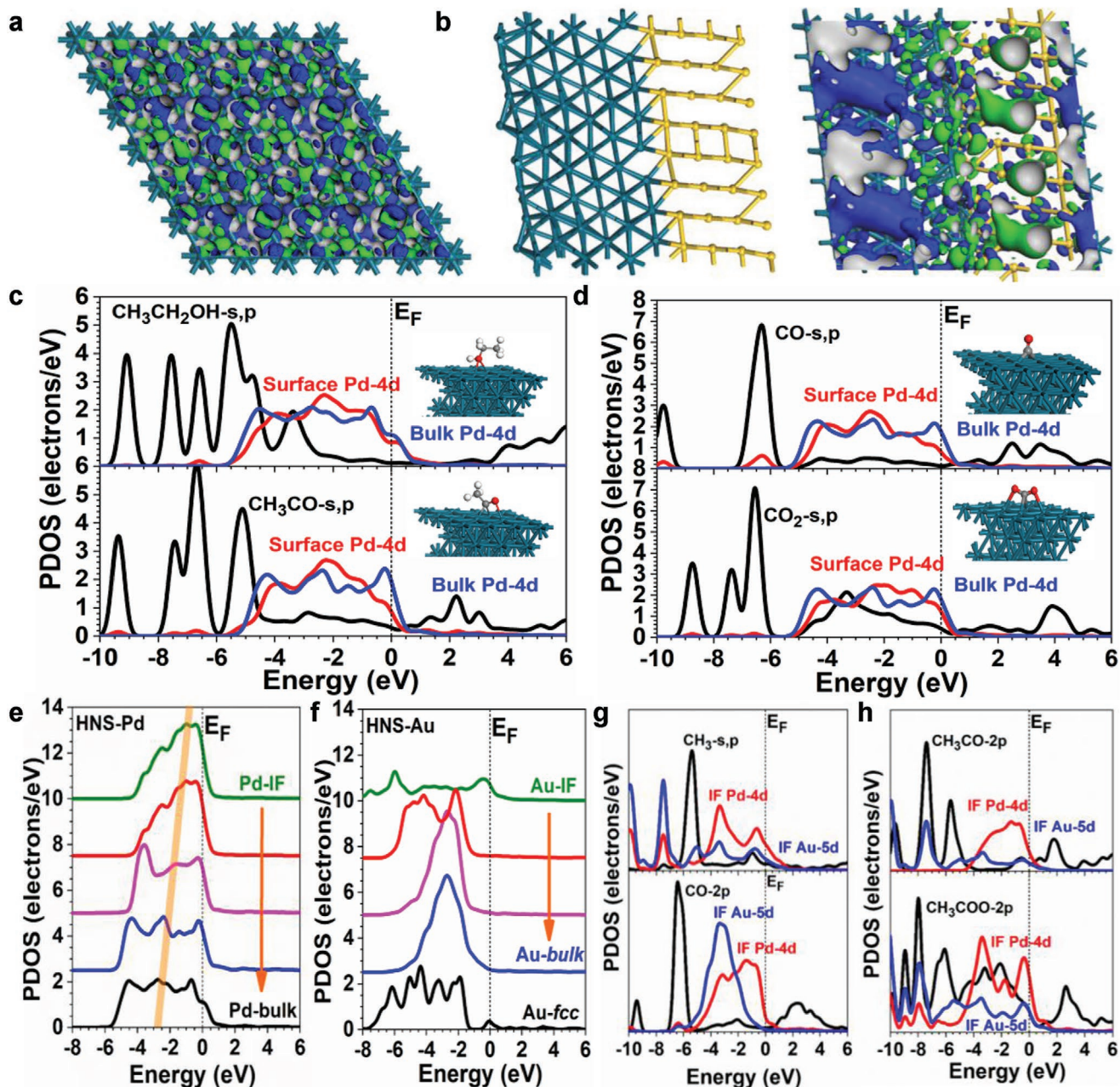


Figure 4. Electronic properties of Pd NS and Pd–Au HNS. a) The real-spatial contour plots for the bonding and antibonding orbitals near the E_F on Pd NSs. b) The real-spatial contour plots for the bonding and antibonding orbitals near the E_F on Pd–Au HNS. c) The PDOSs comparison of the adsorption of $\text{CH}_3\text{CH}_2\text{OH}$ and CH_3CO on the Pd NSs. d) The PDOSs comparison of the adsorption of CO and CO_2 on the Pd NSs. e) The site-dependent PDOSs of Pd from interface (IF) regions toward bulk Pd on Pd–Au HNS. f) The site-dependent PDOSs of Au from interface (IF) regions toward metal Au on Pd–Au HNS. g) The PDOS of key adsorption intermediates CH_3 and CO on Pd–Au HNS. h) The PDOS of “selectivity switch” region of CH_3CO and CH_3COO on Pd–Au HNS.

greatly enhanced in the alkaline condition in Pd–Au HNS, which is consistent with the electronic properties (Figure 5c). Near the IF region on Pd–Au HNS, the activation barriers for the C2 pathway are significantly increased. The even larger barrier than that of C1 reaction pathway indicates a “switch off” for the C2 reaction pathway. As CH_3CO is the common intermediate in both pathways, the lower subsequent energy barriers in C1 pathway and higher activation barriers in C2

pathway demonstrate the EOR selectivity on C1 pathway is significantly boosted after the incorporation of Au (Figure 5d). These energy changes in the reaction pathway explain the enhanced C1 selectivity and EOR activity of Pd–Au HNS observed in experimental results. The effect of incorporation of Au clusters activates the interfacial Pd with a “selectivity switch” for EOR, which largely promotes the C1 pathway meanwhile blocking the C2 pathway.

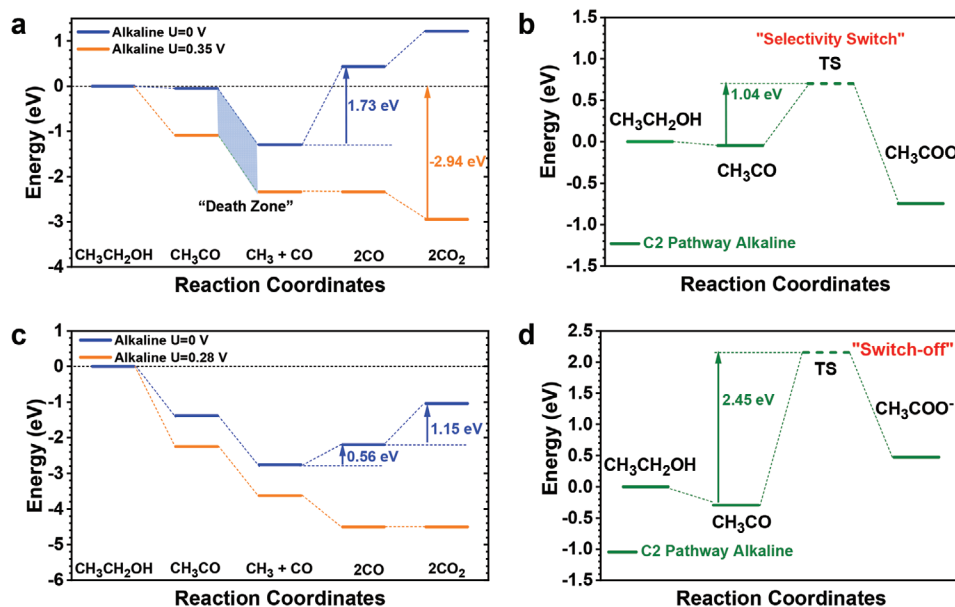


Figure 5. Free energy diagram of C1 and C2 reaction pathway in Pd NS and Pd–Au HNS. a) The energy diagram of C1 reaction pathway on Pd NS. b) The energy diagram of C2 reaction pathway on Pd NS. c) The energy diagram of C1 reaction pathway on Pd–Au HNS. d) The energy diagram of C2 reaction pathway on Pd–Au HNS.

3. Conclusions

In summary, we designed and synthesized a new class of 2D Pd–Au HNS with unique amorphous Pd domain/crystalline Au cluster interphase as an extraordinarily active and stable electrocatalyst toward EOR. Owing to the unique 2D heterophase structure for electronic structure tuning, the Pd–Au HNS/C shows a very high C1 pathway selectivity (FE = 33.2%), showing an order of magnitude higher than that of commercial Pd/C. The Pd–Au HNS/C demonstrates excellent electrocatalysis for EOR with a mass activity of $9.1 \text{ A mg}^{-1} \text{ Pd}$, a long-term stability with 89% mass activity retained after ADT of 2000 potential cycles, outperforming those of pure Pd NS/C and commercial Pd/C. Uncovered by in situ FTIR measurements and EOR products detections, the Pd–Au HNS/C catalyst has a much higher C1 selectivity than Pd NS/C and commercial Pd/C toward EOR, and the break of C–C bond on Pd–Au HNS/C took place at a more low potential than that on Pd NS/C. The theoretical calculations also interpret the substantial effect by the Au introduction to proceed the C1 pathway based on the synergistic effect between electron pump Pd and electron mediator Au at the interfacial region.

4. Experimental Section

Preparation of Pd NS: In a typical preparation of Pd NS, 10 mg of Pd(acac)₂, 20 mg of NH₄Br, 20 mg of W(CO)₆, and 5 mL of OAM were added into a 20 mL vial and ultrasonicated to get the homogeneous solution. After the vial was sealed, the mixture was heated to 80 °C and maintained at this temperature for 1 h in the oven. The cooled product was washed three times with a cyclohexane/ethanol mixture (v:v, 5:1) to wash off the redundant OAM and collected by centrifugation at 8500 rpm.

Preparation of Pd–Au HNS: The collected Pd NS (30 mg) was redispersed in a mixture of 20 mL of 1-octadecene (ODE) and 5 mL of OAM by magnetic stirring. Under a gentle flow of Ar, a controlled amount

of HAuCl₄ predissolved in a mixture of 1.2 mL of ODE and 0.8 mL of OAm was injected. The solution was heated to 80 °C and kept at this temperature for 3 h. The final product was washed three times with a cyclohexane/ethanol mixture (v:v, 5:1) and then dispersed in hexane.

Preparation of Carbon-Supported Catalysts: 5 mg of prepared Pd NS or Pd–Au HNS was dispersed in 60 mL of cyclohexane and then mixed with 20 mg of vulcan XC-72 carbon suspended in 10 mL of ethanol, followed by sonicating for 60 min. After being centrifuged and washed for three times with ethanol, the collected products were dried at 70 °C overnight.

Electrochemical Measurement: The carbon-supported catalysts were dispersed in a mixture containing water, isopropanol, and 5 wt% Nafion (volume ratio: 0.75:0.245:0.005) to form a homogeneous ink by sonication for 60 min in an ice bath. The concentration of precious metal was determined based on the ICP-AES measurement. Electrochemical tests were performed using CHI660E electrochemical workstation (Chenhua, Shanghai) with a three-electrode system. The catalyst modified glass carbon (GC) electrode (Pine Ins) was used as the working electrode, a Hg/Hg₂Cl₂ (in base) electrode was used as the reference electrode, and a Pt wire was used as counter electrode. The potential was calibrated to E(RHE, reversible hydrogen electrode) from E(SCE, saturated calomel electrode) by following the formula $E(\text{RHE}) = E(\text{SCE}) + 0.248 + 0.05916 \cdot \text{pH}$. All the measurements were conducted at room temperature. The working electrodes were first activated by cycling between 0.05 and 1.2 V at 500 mV s⁻¹ in N₂-saturated 1 M KOH. Afterward, for the EOR measurement, the working electrodes were subject to CV scans between 0.05 and 1.2 V at 50 mV s⁻¹ in 1.0 M KOH and 1.0 M ethanol. The mass activity and specific activity were normalized by the mass of Pd metal (determined by the ICP tests) and electrochemically active surface area (ECSA) of catalysts (determined by integrating the Pd reduction peak in CV). For EOR stability test, the accelerated degradation test was conducted by continuous cycling between 0.05 and 1.2 V at the scan rate of 500 mV s⁻¹ in 1.0 M KOH and 1.0 M ethanol. The CV curves were collected after every 500 cycles at the scan rate of 50 mV s⁻¹. The chronoamperometry measurements were conducted at 0.7 V in the same solution. Meanwhile, the solution was refreshed after 5000 s for several times. For the CO stripping tests, the CO oxidation experiments were carried out in 0.1 M KOH solution. Before the test, the solution was purged with argon for 30 min, and then bubbled with CO

gas (99.9%) for 15 min at 0.1 V to achieve the maximum coverage of CO at the Pd active centres. The residual CO in the solution was excluded by argon for 30 min. The ECSA was determined by integrating the charge of Pd reduction. All the electrochemical data were tested for at least three times.

Electrochemical In Situ FTIR Reflection Spectroscopy: Electrochemical in situ FTIR reflection spectroscopy was carried out on a Bruker 70V FTIR spectrometer equipped with a liquid-nitrogen-cooled MCT-A detector. Based on a home-made three-electrode thin-layer IR cell configuration, an IR radiation sequentially passed through a CaF₂ window and a thin-layer solution, and then it was reflected by the electrode surface. The resulting spectra were reported as relative change in reflectivity: $\Delta R/R = (R(E_S) - R(E_R))/R(E_R)$. The $R(E_S)$ and $R(E_R)$ are the single-beam spectra collected at sample potential E_S and reference potential E_R , respectively. Therefore, the downward bands in the spectra indicate the formation of products, while upward bands denote the consumption of reactants. The E_R was fixed at 0.1 V versus RHE. The working electrode was coated with the synthesized catalysts, and the solution is 0.1 M KOH + 0.5 M ethanol.

Before the IR data collection, a clean procedure was applied to the working electrode. The electrode potential was first held at 1.4 V for 5.0 s to completely oxidize any adsorbates, then stepped negatively to -0.10 V. Then the working electrode was pushed against the CaF₂ IR window to form a thin-layer solution. Prior to spectral collection at each E_S , the working electrode was uplifted and cleaned by using the above clean procedure and then pushed down to the IR window to form a thin layer with the renewed solution. To improve the signal-to-noise ratio (S/N), 128 interferograms were collected for each resulting spectrum at different E_S . The spectral resolution was 8 cm⁻¹.

Calculation Setup: All the calculations were performed by the DFT within the CASTEP codes. The generalized gradient approximation (GGA) was applied in the parameterization of Perdew–Burke–Ernzerhof (PBE) for the exchange–correlation energy with the 380 eV cut-off energy. For all the geometry optimizations, the Hellmann–Feynman forces will be converged to less than 0.001 eV Å⁻¹ while the total energy was converged to 5 × 10⁻⁵ eV per atom. The gamma k-point was applied for the energy minimization based on the Broyden–Fletcher–Goldfarb–Shannon (BFGS) algorithm. For a full relaxation of the local lattice within adsorption, a 15 Å vacuum space along z-direction to supply sufficient space was introduced.

Supporting Information

Supporting Information is available from the Wiley Online Library or from the author.

Acknowledgements

F.L. and W.Z. contributed equally to this work. This study was financially supported by Beijing Natural Science Foundation (JQ18005), National Science Fund for Distinguished Young Scholars (No. 52025133), Tencent Foundation through the XPLORER PRIZE, National Key Research and Development Program of China (2017YFA0206701), and the Fund of the State Key Laboratory of Solidification Processing in NWPU (Grant No. SKLSP202004).

Conflict of Interest

The authors declare no conflict of interest.

Data Availability Statement

Research data are not shared.

Keywords

Cl selectivity, ethanol electrooxidation, heterogeneous, interface, nanosheets

Received: January 18, 2021

Revised: February 28, 2021

Published online: April 2, 2021

- [1] C. Bianchini, P. K. Shen, *Chem. Rev.* **2009**, *109*, 4183.
- [2] Z. Xia, X. Zhang, H. Sun, S. Wang, G. Sun, *Nano Energy* **2019**, *65*, 104048.
- [3] J. Bai, D. Liu, J. Yang, Y. Chen, *ChemSusChem* **2019**, *12*, 2117.
- [4] M. Z. F. Kamarudin, S. K. Kamarudin, M. S. Masdar, W. R. W. Daud, *Int. J. Hydrogen Energy* **2013**, *38*, 9438.
- [5] Z. Zhang, Q. Wu, K. Mao, Y. Chen, L. Du, Y. Bu, O. Zhuo, L. Yang, X. Wang, Z. Hu, *ACS Catal.* **2018**, *8*, 8477.
- [6] C. Lafforgue, A. Zadick, L. Dubau, F. Maillard, M. Chatenet, *Fuel Cells* **2018**, *18*, 229.
- [7] L. Chen, L. Lu, H. Zhu, Y. Chen, Y. Huang, Y. Li, L. Wang, *Nat. Commun.* **2017**, *8*, 14136.
- [8] B.-W. Zhang, H.-L. Yang, Y.-X. Wang, S.-X. Dou, H.-K. Liu, *Adv. Energy Mater.* **2018**, *8*, 1703597.
- [9] W. Zhang, Y. Yang, B. Huang, F. Lv, K. Wang, N. Li, M. Luo, Y. Chao, Y. Li, Y. Sun, Z. Xu, Y. Qin, W. Yang, J. Zhou, Y. Du, D. Su, S. Guo, *Adv. Mater.* **2019**, *31*, 1805833.
- [10] H. Xu, H. Shang, C. Wang, Y. Kou, *Adv. Funct. Mater.* **2020**, *30*, 2000793.
- [11] H. Xu, H. Shang, C. Wang, Y. Kou, *Small* **2021**, *17*, 2005092.
- [12] H. Xu, H. Shang, C. Wang, Y. Kou, *Adv. Funct. Mater.* **2020**, *30*, 2006317.
- [13] Y. Wang, S. Zou, W.-B. Cai, *Catalysts* **2015**, *5*, 1507.
- [14] X. Yu, Z. Luo, T. Zhang, P. Tang, J. Li, X. Wang, J. Llorca, J. Arbiol, J. Liu, A. Cabot, *Chem. Mater.* **2020**, *32*, 2044.
- [15] H. Mistry, A. S. Varela, S. Kühn, P. Strasser, B. R. Cuenya, *Nat. Rev. Mater.* **2016**, *1*, 16009.
- [16] S. C. Lai, M. T. Koper, *Phys. Chem. Chem. Phys.* **2009**, *11*, 10446.
- [17] W. Du, G. Yang, E. Wong, N. A. Deskins, A. I. Frenkel, D. Su, X. Teng, *J. Am. Chem. Soc.* **2014**, *136*, 10862.
- [18] C. Zhu, B. Lan, R.-L. Wei, C.-N. Wang, Y.-Y. Yang, *ACS Catal.* **2019**, *9*, 4046.
- [19] R. Rizo, R. M. Aran-Ais, E. Padgett, D. A. Muller, M. J. Lazaro, J. Solla-Gullon, J. M. Feliu, E. Pastor, H. D. Abruna, *J. Am. Chem. Soc.* **2018**, *140*, 3791.
- [20] W. Huang, X. Y. Ma, H. Wang, R. Feng, J. Zhou, P. N. Duchesne, P. Zhang, F. Chen, N. Han, F. Zhao, J. Zhou, W. B. Cai, Y. Li, *Adv. Mater.* **2017**, *29*, 1703057.
- [21] M. Li, D. A. Cullen, K. Sasaki, N. S. Marinkovic, K. More, R. R. Adzic, *J. Am. Chem. Soc.* **2012**, *135*, 132.
- [22] L. Bu, S. Guo, X. Zhang, X. Shen, D. Su, G. Lu, X. Zhu, J. Yao, J. Guo, X. Huang, *Nat. Commun.* **2016**, *7*, 11850.
- [23] M. Sial, H. Lin, M. Zulfiqar, S. Ullah, B. Ni, X. Wang, *Small* **2017**, *13*, 1700250.
- [24] A. Kowal, M. Li, M. Shao, K. Sasaki, M. B. Vukmirovic, J. Zhang, N. S. Marinkovic, P. Liu, A. I. Frenkel, R. R. Adzic, *Nat. Mater.* **2009**, *8*, 325.
- [25] H. Lv, Y. Wang, A. Lopes, D. Xu, B. Liu, *Appl. Catal., B* **2019**, *249*, 116.
- [26] S. Shen, Y. Guo, L. Luo, F. Li, L. Li, G. Wei, J. Yin, C. Ke, J. Zhang, *J. Phys. Chem. C* **2018**, *122*, 1604.
- [27] H. Lin, M. Muzzio, K. Wei, P. Zhang, J. Li, N. Li, Z. Yin, D. Su, S. Sun, *ACS Appl. Energy Mater.* **2019**, *2*, 8701.
- [28] W. Huang, X. Kang, C. Xu, J. Zhou, J. Deng, Y. Li, S. Cheng, *Adv. Mater.* **2018**, *30*, 1706962.
- [29] H. A. Asiri, A. B. Anderson, *J. Electrochem. Soc.* **2014**, *162*, F115.

- [30] K. D. Gilroy, A. Ruditskiy, H. C. Peng, D. Qin, Y. Xia, *Chem. Rev.* **2016**, *116*, 10414.
- [31] X. Zhang, C. Lian, Z. Chen, C. Chen, Y. Li, *Nano Res.* **2018**, *11*, 4142.
- [32] H. Zhang, T. Watanabe, M. Okumura, M. Haruta, N. Toshima, *Nat. Mater.* **2011**, *11*, 49.
- [33] H. Cheng, N. Yang, G. Liu, Y. Ge, J. Huang, Q. Yun, Y. Du, C. J. Sun, B. Chen, J. Liu, H. Zhang, *Adv. Mater.* **2020**, *32*, 1706962.
- [34] S. Xue, W. Deng, F. Yang, J. Yang, I. S. Amiinu, D. He, H. Tang, S. Mu, *ACS Catal.* **2018**, *8*, 7578.
- [35] Y. Wu, D. Wang, G. Zhou, R. Yu, C. Chen, Y. Li, *J. Am. Chem. Soc.* **2014**, *136*, 11594.
- [36] B. Narayanamoorthy, K. K. R. Datta, M. Eswaramoorthy, S. Balaji, *ACS Catal.* **2014**, *4*, 3621.
- [37] Z.-Y. Zhou, Q. Wang, J.-L. Lin, N. Tian, S.-G. Sun, *Electrochim. Acta* **2010**, *55*, 7995.
- [38] J. Zhang, J. Ye, Q. Fan, Y. Jiang, Y. Zhu, H. Li, Z. Cao, Q. Kuang, J. Cheng, J. Zheng, Z. Xie, *J. Am. Chem. Soc.* **2018**, *140*, 11232.
- [39] M. Farsadrooh, J. Torrero, L. Pascual, M. A. Peña, M. Retuerto, S. Rojas, *Appl. Catal., B* **2018**, *237*, 866.
- [40] E. A. Monyoncho, S. N. Steinmann, C. Michel, E. A. Baranova, T. K. Woo, P. Sautet, *ACS Catal.* **2016**, *6*, 4894.
- [41] Y.-Y. Yang, J. Ren, Q.-X. Li, Z.-Y. Zhou, S.-G. Sun, W.-B. Cai, *ACS Catal.* **2014**, *4*, 798.
- [42] H. Li, Q. Fan, J. Ye, Z. Cao, Z. Ma, Y. Jiang, J. Zhang, J. Cheng, Z. Xie, L. Zheng, *Mater. Today Energy* **2019**, *11*, 120.